



Abnormal grain growth of UO_2 with pores in the final stage of sintering: A phase field study

Yaolin Guo^a, Zhen Liu^a, Qing Huang^a, Cheng-Te Lin^b, Shiyu Du^{a,*}

^a Engineering Laboratory of Specialty Fibers and Nuclear Energy Materials (FINE), Ningbo Institute of Materials Technology and Engineering, Chinese Academy of Sciences, Ningbo, Zhejiang 315201, China

^b Key Laboratory of Marine Materials and Related Technologies, Zhejiang Key Laboratory of Marine Materials and Protective Technologies, Ningbo Institute of Materials Technology and Engineering, Chinese Academy of Sciences, Ningbo, Zhejiang, China

ARTICLE INFO

Article history:

Received 20 October 2017

Received in revised form 21 December 2017

Accepted 22 December 2017

Available online 30 December 2017

Keywords:

UO_2

Sintering

Phase field

Abnormal grain growth

Pores

Grain boundary

ABSTRACT

The phase field formulation has been employed to investigate the abnormal grain growth behaviors for UO_2 with pores in the final stage of sintering. The microstructure evolution is found dependent on the total volume fraction and individual sizes of pores. The grain growth rate is evidently suppressed when the porosity is high and it is found independent of pore size at low porosity. Moreover, the smaller pores may cause worse abnormal grain growth at low porosities and more significant stagnation effect at high porosities in the sintering of UO_2 . By further inspection on pore-boundary interaction in a bi-grain system designed in this work, the grain growth behavior is determined to be strongly correlated to the engulfment of pores by grains which may be described by the critical grain radius and critical time defined hereby. The data obtained may provide a new insight into the mechanism behind the sintering technology of nuclear fuels such as UO_2 .

© 2018 Elsevier B.V. All rights reserved.

1. Introduction

As the most widely utilized nuclear fuel at present, UO_2 is of great importance in nuclear industry. The microstructure of UO_2 plays a decisive role in its performance in a nuclear reactor. By theories and experiments, it has been reported that UO_2 with large grains can suppress the emission of fission gas during operation of the reactor, assisting to enhance the burn-up and extend the operating life of the fuel [1]. Therefore, in order to improve the performance of UO_2 , one of the effective ways is the preparation of UO_2 with uniformly distributed large grains, which demands elaboration on the fabrication procedures, such as sintering. Nowadays, the investigation on UO_2 grain growth behaviors during the sintering process has attracted considerable attention. Particularly, the understanding of grain growth behavior in the final stage of sintering, which is significantly influenced by the interaction between the grain boundaries (GBs) and pores, is crucial to control the microstructure of UO_2 pellets.

Since 1960s, many studies have been reported on the grain growth of UO_2 during the process of sintering. Ainscough et al. [2] studied the isothermal grain growth kinetics of sintered UO_2

pellets, and found temperature had impact on the grain size limit. MacEwan et al. [3] claimed that pronounced grain growth was not observed in sintering processes until the total porosity decreased to 2–3% of the volume for the specimens. Brook [4] studied the interaction between GBs and pores and found that different mechanisms of pore-boundary interaction could lead to different grain growth exponents. During the sintering of UO_2 , various ways of mass transport including surface, GB and bulk diffusion and evaporation-condensation (EC) can facilitate the pore-boundary interaction dependent on temperatures [5–8]. Bourgeois et al. [9] found surface diffusion was the predominant transport mechanism over EC for pore migration at around 1700 °C. Depending on the mechanisms of pore-boundary interaction, grain size distribution and sintering atmosphere, the grain growth behavior can be normal or abnormal [10]. Normal grain growth (NGG) is driven by the decrease of total grain boundary energy and evolves in a uniform manner. On the contrary, abnormal grain growth (AGG) is characterized by a subset of grains gaining some privilege to grow faster than others and tends to result in non-uniform microstructure. In fact, the anisotropy in the GB energy, GB mobility [11], GB complexion [12], free surfaces [13] and second phase particle distributions [14] may synergistically induce AGG. For polycrystalline materials, occurrence of AGG often has undesirable effects on the homogeneity of grain size [15]. During the final stage of

* Corresponding author.

E-mail address: dushiyu@nimte.ac.cn (S. Du).

UO₂ sintering, especially, pores located at GBs are likely to alter the motion of the GBs, leading to the occurrence of AGG the degree of which is dependent on the distribution of pore sizes and locations [5]. Bourgeois et al. [16] found that grain growth in the final stage of sintering of UO₂ could be considered as abnormal in the sense that the pores does not seem to pin the GBs. However, it is still an open question what impact the pore distribution has on AGG of UO₂.

To study the UO₂ grain growth behavior with pores, a number of methods have been adopted experimentally and theoretically. With the rapid development of super-computing, numerical modelling has become a major technique in this field recently. In particular, the phase field model is considered as a promising scheme to describe the microstructure evolution of UO₂ with pores from different perspectives, such as pore-boundary interaction during UO₂ GB migration [17], fission gas bubble evolution in UO₂ under post-irradiation thermal annealing [18], and features of faceted void morphologies in UO₂ [19]. Especially, Ahmed et al. [5–8] have recently developed a phase field model and accurately obtained the kinetics of grain growth in porous UO₂. This model can combine various diffusion mechanisms concerning the interaction between GB and pores. Moreover, by this model one can incorporate the GB diffusivity and surface diffusivity with respect to the specific material, such as UO₂. The predictions exhibit excellent agreement with the experimental results, demonstrating that this model is suitable to explore the porous grain growth. Nevertheless, the role of pore distributions in the AGG of UO₂ during the final stage of sintering has not been thoroughly studied and needs further investigation.

In this article, we use the phase field model to study the grain growth behavior of UO₂ with pores in the final stage of sintering, with emphasis on the characteristics of AGG. The roles of total pore volume fraction and individual pore size in AGG are elucidated. Particularly, to characterize the degree of abnormality for AGG, a five-level hierarchy system based on grain sizes is thereby applied.

2. Phase field model

Here, the phase field modeling in the framework provided by Ahmed et al. [5–8] is employed to study the microstructure evolution of UO₂. The free energy functional F for the non-uniform medium consisting of solid grains and pores is given as follows:

$$F = \int \left[f(\rho, \eta_1, \eta_2, \dots, \eta_q) + \frac{k_\rho}{2} |\nabla \rho|^2 + \frac{k_\eta}{2} \sum_{\alpha=1}^q |\nabla \eta_\alpha|^2 \right] d^3 \mathbf{r}. \quad (1)$$

Here $\rho(\mathbf{r}, t)$ is the conserved field as the function of position vector \mathbf{r} and time t to distinguish grains ($\rho = 1$) and pores ($\rho = 0$). η_α ($\alpha = 1, 2, \dots, q$) are the non-conserved order parameters with q as the total number of grains, being unity in the α -th grain and zero otherwise to distinguish different grains. The changes in these parameters reflect the microstructure evolution in the polycrystalline solid with pores [6]. k_ρ and k_η are the gradient coefficients. Consistent with Ahmed et al. [5–8], the bulk free energy density f is

$$f(\rho, \eta_1, \eta_2, \dots, \eta_q) = B\rho^2(1 - \rho)^2 + C \left[\rho^2 + 6(1 - \rho) \sum_{\alpha=1}^q \eta_\alpha^2 - 4(2 - \rho) \sum_{\alpha=1}^q \eta_\alpha^3 + 3 \left(\sum_{\alpha=1}^q \eta_\alpha^2 \right)^2 \right]. \quad (2)$$

As discussed below, B and C , along with k_ρ and k_η in Eqs. (1) and (2), are structure-related constants determined by surface, GB energies and GB width. The free energy parameters are related to the material properties as [6]:

$$\begin{aligned} \gamma_{GB} &= 2\sqrt{Ck_\eta/3}, \\ \gamma_s &= \sqrt{2(k_\rho + k_\eta)(B + 7C)}/6, \\ l &= \sqrt{4k_\eta/3C} = \delta, \\ 6k_\rho C &= k_\eta(B + C), \end{aligned} \quad (3)$$

where γ_{GB} , γ_s and δ are the GB energy, surface energy, and GB width, respectively, and l is the diffuse interface width. In our simulation, specifically, for UO₂ with surface energy γ_s of 0.6 J/m², GB energy γ_{GB} of 0.3 J/m² and GB width δ of 1 nm [6], the free energy parameters take on the values: $B = 1.9176 \times 10^9$ J/m³, $C = 1.128 \times 10^8$ J/m³, $k_\eta = 6 \times 10^{-10}$ J/m and $k_\rho = 1.8 \times 10^{-9}$ J/m. According to the empirical potential calculations, the GB energy of UO₂ may be in the range of 1–1.9 J/m² at 0 K [20]. However, the GB energy can be largely decreased with the increasing temperature, especially at high temperatures, for example, above 0.5T_m in oxides [21,22] and metals [23]. In experiments, the sintering temperatures can be actually around 1700 °C [16,24]. Furthermore, the surface diffusion activation data obtained by experiments are relatively reliable between 1200 °C and 1800 °C [9]. Thus, 1700 °C is chosen as the sintering temperature in the current modelling study, which is close to 0.6 T_m. As a result, it is reasonable to choose GB energy to be 0.3 J/m² consistent with the previous simulations and experiments [6,24].

The governing equations for the field and order parameters are given by:

$$\begin{aligned} \frac{\partial \rho}{\partial t} &= \nabla \cdot \mathbf{M} \nabla \frac{\delta F}{\delta \rho}, \\ \frac{\partial \eta_\alpha}{\partial t} &= -L \frac{\delta F}{\delta \eta_\alpha}. \end{aligned} \quad (4)$$

In Eq. (4), L is Allen-Cahn mobility; $\delta F/\delta \rho$ and $\delta F/\delta \eta_\alpha$ are functional derivatives of the free energy with respect to ρ and η_α . $\mathbf{M} = \mathbf{D}v_m/RT$ is the chemical mobility tensor, with \mathbf{D} as the mass diffusion tensor, $v_m = 24.5 \times 10^{-6}$ m³/mol as the molar volume, R as the universal gas constant and T as the absolute temperature. This tensor accounts for multiple diffusion mechanisms, including bulk, GB and surface diffusions [5]. According to Ahmed et al. [6], surface diffusion is the dominant mechanism in the sintering of UO₂ at high temperatures and will be also considered as the major mechanism in our simulation. For UO₂ with only surface diffusion, $\mathbf{M} = v_m \mathbf{D}_s/RT$ with \mathbf{D}_s as the surface diffusion tensor along the surface of pores. Specifically, $\mathbf{D}_s = D_s \rho^2 (1 - \rho^2) \mathbf{T}_s$, where D_s is the surface diffusion coefficient, chosen as $D_s = 50 \exp(-450,000/RT)$ [24] and $\mathbf{T}_s = \mathbf{I} - \mathbf{n}_s \otimes \mathbf{n}_s$ with \mathbf{I} being the identity tensor, \otimes representing the dyadic product, and \mathbf{n}_s the unit normal vector to the pore surface, calculated by $\mathbf{n}_s = \nabla \rho / |\nabla \rho|$. In order to determine L in Eq. (4), a relation of $L = \gamma_{GB} M_{GB}/k_\eta$ will be used, where $M_{GB} = D_a v_m/RT\delta$ is the GB migration mobility with GB migration coefficient $D_a = 1.38 \times 10^{-7} \exp(-239,000/RT)$, which has been proved to be suitable for describing grain growth of UO₂ [6]. The key expressions used for calculating \mathbf{M} and L in Eq. (4) are summarized in Table 1.

To implement convenient numerical governing equations, the coefficients k_ρ , k_η , B and C are simultaneously rescaled according to Eq. (3) to allow for the use of much thicker diffusive interface l (e.g. $l = 1.3 \mu\text{m}$ in this article) while keeping the surface and GB energies as well as the grain growth kinetics invariant [6]. Thus, the dimensionless version of the kinetic equations is constructed by choosing $\varepsilon = B'$ (rescaled B), $l^* = 0.2l'$ and $t^* = 1/Le$ as the reference energy density, length scale and time scale, respectively, expressed as follows [6]

Table 1
Key expressions for the calculation of \mathbf{M} and L .

Description	Symbol	Expression	Unit
Chemical mobility tensor	\mathbf{M}	$\mathbf{M} = v_m \mathbf{D}_s / RT$	$\text{m}^5 / \text{J} \cdot \text{s}$
Surface diffusion tensor	\mathbf{D}_s	$\mathbf{D}_s = D_s \rho^2 (1 - \rho^2) \mathbf{T}_s$	m^2 / s
Surface diffusion coefficient	D_s	$D_s = 50 \exp(-450,000/RT)$	m^2 / s
Phase field mobility	L	$L = \gamma_{GB} M_{GB} / k_\eta$	$\text{m}^3 / \text{J} \cdot \text{s}$
GB mobility	M_{GB}	$M_{GB} = D_a v_m / RT \delta$	$\text{m}^4 / \text{J} \cdot \text{s}$
GB migration coefficient	D_a	$1.38 \times 10^{-7} \exp(-239,000/RT)$	m^2 / s
GB diffusion coefficient	D_{GB}	$1.38 \times 10^{-6} \exp(-239,000/RT)$	m^2 / s

$$\frac{\partial \rho}{\partial \tau} = l^* \nabla \cdot \frac{\mathbf{M}}{L l^2} l^* \nabla \frac{1}{\varepsilon} \frac{\delta F}{\delta \rho} = \tilde{\nabla} \cdot \tilde{\mathbf{M}} \tilde{\nabla} \frac{\delta \tilde{F}}{\delta \rho}, \quad (5)$$

$$\frac{\partial \eta_\alpha}{\partial \tau} = -\frac{1}{\varepsilon} \frac{\delta F}{\delta \eta_\alpha} = -\frac{\delta \tilde{F}}{\delta \eta_\alpha},$$

where $\tau = t/t^*$, $\tilde{\nabla} = l^* \nabla$ and $\tilde{\mathbf{M}} = \mathbf{M}/L l^2$ are dimensionless time, delta operator and chemical mobility, respectively. To solve the above equations, finite difference algorithms are used in both equations. In our simulations, periodic boundary conditions are applied in all three dimensions, the spatial step $\Delta x = l^* = 0.27 \mu\text{m}$, and explicit time integration are used with the time step $\Delta t = 0.1 = 0.27 \text{ s}$. In the numerical implement, we use up to 8 phase field components to fully simulate the grain growth with the approach proposed by Kim et al. [25] to lower the computational expense.

Initially, there are 377 grains constructed by Voronoi tessellation method [26] with evenly distributed grain size which is represented by the grain radius R_g , calculated by directly averaging the distances from the GB points to the grain centroid. Initial grain size R_0 is nearly $22\Delta x \approx 5.9 \mu\text{m}$, and the initial spherical pores with the equal radius r_p are randomly distributed at GBs and GB junctions. Considering the initial Voronoi grains are not in equilibrium with each other, about 0.5 h will be regarded as an initial transient period to let the junctions of grain-grain and pore-grain reach equilibrium. The grain growth behaviors of UO_2 will be investigated and compared in terms of different groups sorted by porosity f_p with different r_p selected in the set $\{0, 7, 8, 10, 12, 14\}\Delta x$. Specifically, f_p values labelled by six groups (No. 0, 1, 2, 3, 4, 5) are 0, 0.6%, 1.3%, 2.6%, 3.8% and 5.1%, respectively, corresponding to six different initial pore numbers N_p , i.e., $N_p = 0, 50, 100, 200, 300$ and 400 with $r_p = 8\Delta x$, as shown in Table 2. For the sake of statistical rationality, the simulations will not cease until the number of grains in the simulation domain reduces to less than 1/5 of the initial value.

3. Results

Fig. 1 shows two snapshots of three-dimensional (3D) microstructure represented by $\tilde{\eta} = \sqrt{\sum_\alpha \eta_\alpha^2}$ with $N_p = 100$ and $r_p = 8\Delta x$ at the moments of 0.8 h and 1.5 h, when the local equilibrium has been achieved between the pores and the nearby GBs.

Table 2
Groups with different pore distributions ($r_p = 8\Delta x$).

Group no.	Porosity f_p	N_p ($r_p = 8\Delta x$)
0	0	0
1	0.6%	50
2	1.3%	100
3	2.6%	200
4	3.8%	300
5	5.1%	400

The pores are located on GBs and TJs in the shape of irregular polygons, and the grain sizes are relatively small as shown in Fig. 1(a). As the sintering time evolves, grain growth occurs with the shape changes in pores, as displayed in Fig. 1(b). During the whole sintering time, pore-pore interaction is allowed which occurs when the pores are close enough to each other. Nevertheless, the pore-pore interaction via surface diffusion imposes perceivable effect on the dynamics of grain growth since the dynamics of surface diffusion is too slow. In the following content, the dependence of UO_2 grain growth behaviors in the final stage of sintering on the pore distributions, including total pore volume and individual pore size, will be illustrated with more details.

Before further analyses, it is necessary to discuss the methods of calculating grain size. If the grains are assumed to be perfectly spherical, the grain radius R_g can be written as

$$R_g = \left(\frac{3V_g}{4\pi} \right)^{1/3}, \quad (6)$$

with V_g the grain volume. However, the actual grain shapes can be more like irregular polygons, such as icosahedron, tetradecahedron and tetrahedron etc., relying on the actual surrounding grains and pores. Clearly, the local boundary shape cannot be taken into account by Eq. (6), limiting its utility in the systems with complex grain shapes due to pores. Instead, we choose to calculate the grain radius directly from averaging the distances between the boundary points and grain centroid. Specifically, the radius $R_{g,i}$ of grain i can be written as

$$R_{g,i} = \frac{1}{N_i^B} \sum_{k=1}^{N_i^B} |\mathbf{r}_i^O - \mathbf{r}_{i,k}^B|, \quad (7)$$

where N_i^B is the number of boundary points containing both of GB and surface points, \mathbf{r}_i^O and $\mathbf{r}_{i,k}^B$ ($k = 1, \dots, N_i^B$) denote the position vectors of the centroid and boundary points of grain i , respectively.

To benchmark our calculating method, the grain radii with pores of $N_p = 100$ and $r_p = 8\Delta x$ at the time of $10000\Delta t$ are compared by these two methods, i.e., R' from Eq. (6) and R'' from Eq. (7). To better visualize the results, all the grains are sorted in the descending order via grain volume and the ratio of $\zeta = R''/R'$ is shown in Fig. 2. If $\zeta = 1$, the grain shape can be approximated as a sphere. If ζ is away from 1, the grain shape may be complex. For the larger grains with, for instance, grain order number less than 50, ζ is very close to 1 with difference of no more than 2.5%, indicating that those grains may be similar with spheres. In fact, the grains in average may be approximated as a tetradecahedron with 14 faces [27,28]. The growing grains can have more faces, which are closer to spheres. Nonetheless, for the smaller grains, the difference between ζ and 1 increases, indicating that those small grains cannot simply be seen as spheres. In the process of grain growth, the smallest grains are often diminishing and shaped by nearby GBs and TJs, resulting in polygon-like grains with less faces, such as tetrahedrons [29]. Therefore, smaller grains cannot be treated as spherical ones. Our calculation method for grain radii can capture the different features of growing and diminishing grains. Furthermore, using our calculation, it is beneficial for the case when many pores are located in grain's interior. In that case, the grain radii using grain volume may bring errors because the GB shape is insensitive to the pores inside the grain. Instead, the grain radius via our method will hardly be affected by the inner pores. Lastly, our method lays a solid foundation for the further analyses.

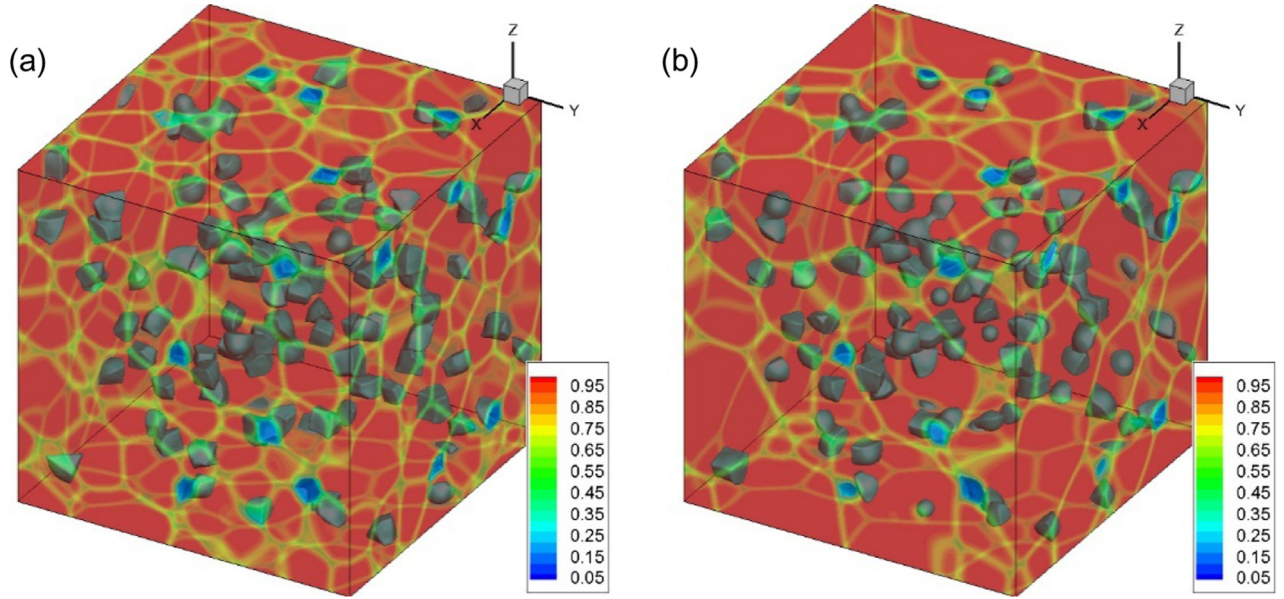


Fig. 1. Snapshots of 3D microstructure represented by $\bar{\eta} = \sqrt{\sum_g \eta_g^2}$ with initial pores of $N_p = 100$ and $r_p = 8\Delta x$ at $t =$ (a) 0.8 h ($10,000\Delta t$) and (b) 1.5 h ($20,000\Delta t$). The red denotes the grain interior ($\bar{\eta} \rightarrow 1.0$), blue represents the pore inside ($\bar{\eta} \rightarrow 0$), and yellow shows the GB ($\bar{\eta} \sim 0.75$). (For interpretation of the references to colour in this figure legend, the reader is referred to the web version of this article.)

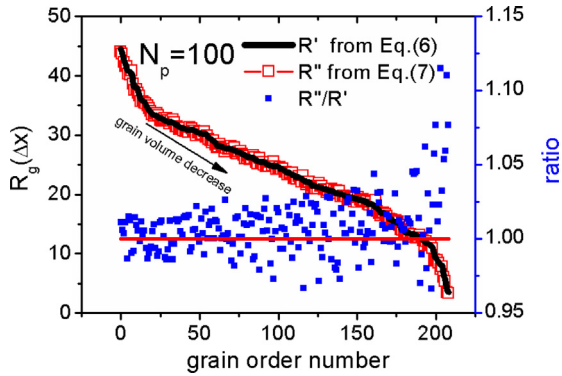


Fig. 2. Directly calculated radii and derived radii from grain volume in the order of decreasing grain volume with $N_p = 100$ and $r_p = 8\Delta x$ when $t = 10,000\Delta t$. The straight line indicates that ratio of $R''/R' = 1$.

3.1. Total pore volume dependence

First, the role of total pore volume with constant pore radius is investigated. Temporal evolution of the average grain radius $R_{g,ave}$ over all the grains is investigated under different N_p with $r_p = 8\Delta x$, as shown in Fig. 3(a). When there are no pores, the grain growth occurs rapidly. The $R_{g,ave}$ value increases by nearly 2.5 times in three hours. With N_p below 100 corresponding to the porosity less than 1.3%, the grain growth dynamics basically resembles that in the case without pores. For the case of $N_p = 200$, the growth rate is close to the pore-free UO_2 when $t < 2.0$ h, but the retarding effect becomes significant afterwards. As to the systems with $N_p > 200$, the decline of the grow rate can be readily identified. For example, when $N_p = 400$ the grain growth is significantly suppressed with the grain size 30% lower than that without pores after 3.5 h. Thus, a high enough porosity can retard the grain growth rate, which is in agreement with Ahmed et al.'s results [6].

To show the grain growth feature, grain growth dynamics without pores is compared with the ideally NGG theory [25], as shown in Fig. 3(b). The classical equation for the ideally NGG is written as

$$R_g^2(t) - R_0^2(t_0) = kt \quad (8)$$

where $R_0(t_0)$ denotes the average grain radius when NGG begins at t_0 , and $R_g(t)$ represents the grain radius at t , $k = M_{GB}\gamma_{GB}/2$, which can be determined as $k^{theory} = 1.455 \times 10^{-2} \text{ } (\mu\text{m}^2/\text{s})$ at $T = 1700^\circ\text{C}$ from Table 1. For convenience, the relation of $R_g^2(t) \sim kt$ is used to verify our result with the theory. The data points of squared grain radius at $N_p = 0$ are linearly fitted with the slope as $(1.3 \pm 0.06) \times 10^{-2} \text{ } (\mu\text{m}^2/\text{s})$, which agrees well with k^{theory} . Furthermore, the linear fittings of the points with $N_p = 50, 100, 200, 300, 400$ show that when N_p increases the grain growth is slowed down. As N_p increases, in fact, the grain growth dynamics may not agree with Eq. (8), i.e., the mechanism of grain growth may have been altered, such as from GB curvature driven ($R^2 \sim t$) to surface diffusion controlled grain growth ($R^4 \sim t$) [7]. However, the change in mechanism of grain dynamics is not the focus of this article, more details have been provided by Ahmed et al. [7].

Subsequently, the changes in the distribution of grains due to the increase in the pore volume is further explored beyond average grain size curves. Fig. 4 shows the cumulative fraction distribution of the grain size normalized by $R_{g,ave}$ for the systems with different N_p . When there are no pores the curves of cumulative fraction coincide at four moments, i.e., 0.8, 1.5, 2.2 and 3.0 h, and can be described by the Weibull distribution functions [29], as shown in Fig. 4(a). This is the embodiment of self-similarities of NGG [25]. Additionally, the maximum $R_g/R_{g,ave}$ is in the vicinity of 1.8, which also complies with the theory of NGG proposed by Hilliert [30]. Thus, to better compare the results of $N_p > 0$ with the $N_p = 0$ case, a standard curve is obtained by averaging the curves at different time in Fig. 4(a). As N_p increases from 50 to 200, there appear apparent discrepancies between the cumulative fraction curves and the standard one, which can be used as an indicator of the occurrence of AGG. In a qualitative view, the discrepancies are significant for N_p in an intermediate range ($N_p = 50$ and $N_p = 100$); while the variation turns lower for larger N_p ($=200$). Comparing the case of $N_p = 50$ to that of $N_p = 100$, the maximum $R_g/R_{g,ave}$ of the former is between 1.8 and 1.9 which is close to the NGG case in Fig. 4(a), whereas that of the latter is almost 2.2. Elaborative inspection for the case $N_p = 100$ also finds that the distribution dif-

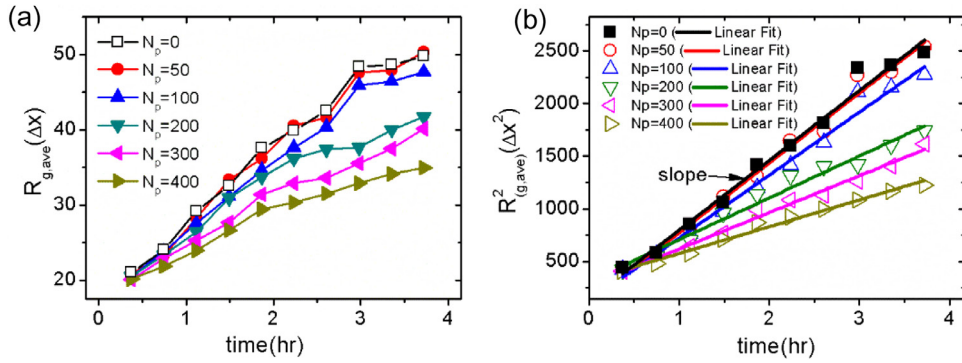


Fig. 3. (a) Temporal evolution of average grain radius $R_{g,ave}$ for different N_p . (b) Squared grain radius versus time and linear fits at different N_p . The slopes of linear fitted curves with $N_p = 0, 50, \dots, 400$ are respectively 0.013, 0.013, 0.018, 0.0078, 0.0068 and 0.0050 ($\mu m^2/s$), compared to 0.014553 ($\mu m^2/s$) calculated from ideally NGG theory. (Number of total pores remains constant except for few pore coalescence due to the initial close distance.)

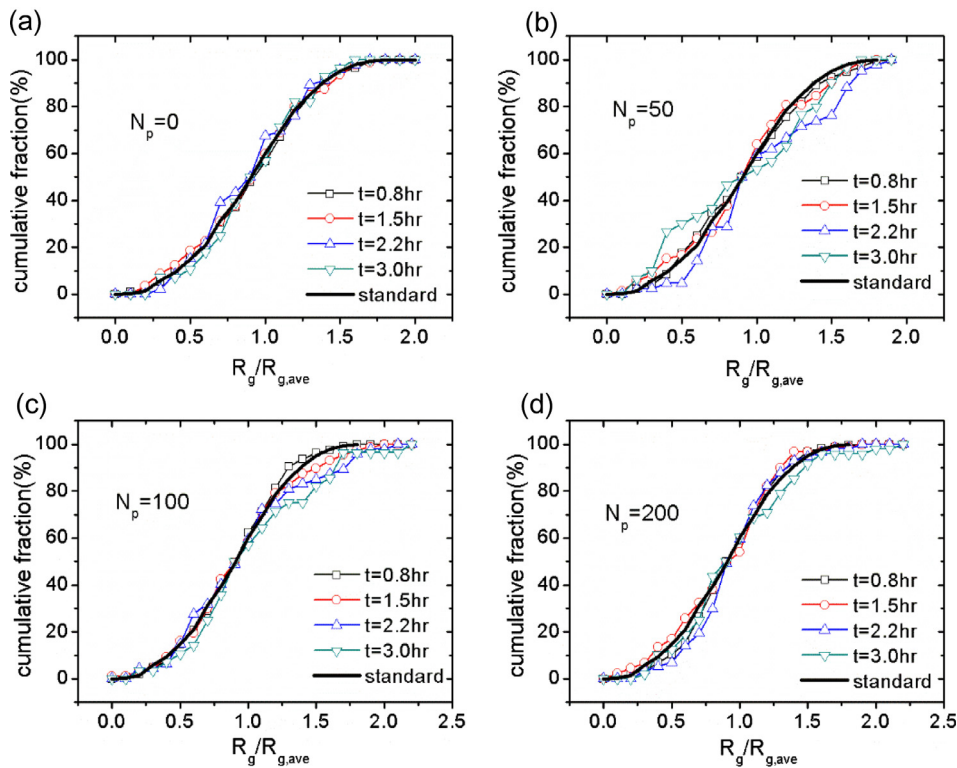


Fig. 4. Cumulative fraction of $R_g/R_{g,ave}$ with pores at $N_p =$ (a) 0, (b) 50, (c) 100, (d) 200.

ference is inconspicuous for small sized grains but is notable for large grains. The maximum is beyond the standard one for both $N_p = 100$ and $N_p = 200$. However, the discrepancies between the curves at discrete time are not sufficient to describe the variation of AGG over the whole sintering time and cannot quantitatively depict it in a convenient way.

To quantitatively and continuously characterize the abnormality of grain growth, all the grains are sorted according to their sizes and correspondingly divided into five equal groups (denoted as level 1–5) with level 1 containing the largest grains. Then, the temporal evolution of grain volume fraction in each level for the systems with different N_p (corresponding to different porosities) are shown in Fig. 5. After the initial equilibrium period of around 0.5 h, the volume fraction in each level remains almost constant for $N_p = 0$ as shown in Fig. 5(a). The fraction for level 1 is determined to be around 50% of all grains and those of other levels drop in the range of [1%, 25%]. For UO_2 with pores, similarities in grain size

distribution by levels to the nonporous system can be readily found. For instance, the grain volume fractions of level 1 are all larger than 45% after the transition period. Furthermore, the variations in the level 2–5 are generally homogeneous for systems with different pore volumes: level 2 is in the range of 20–30%; level 3 in the interval of 10–20%; level 4 and level 5 below 10%. However, the difference in evolution of level 1 in Fig. 5(b–d) is also found comparing to Fig. 5(a). Specifically, the total volume fraction of level 1 has slightly increased to around 53% at $N_p = 50$. For the case of $N_p = 100$, the maximum fraction of level 1 approaches 65%. When N_p is further increased to 200, the fraction initially stays at 50% and then reaches approximately 60%.

Conventionally, the ratio of the grain sizes between the largest one and the average one is adopted to characterize the abnormality when the grain number is low [31]. Nevertheless, when the grain number is beyond hundreds, e.g., in our simulation, this ratio is not sufficient to describe the global grain growth behavior, and is

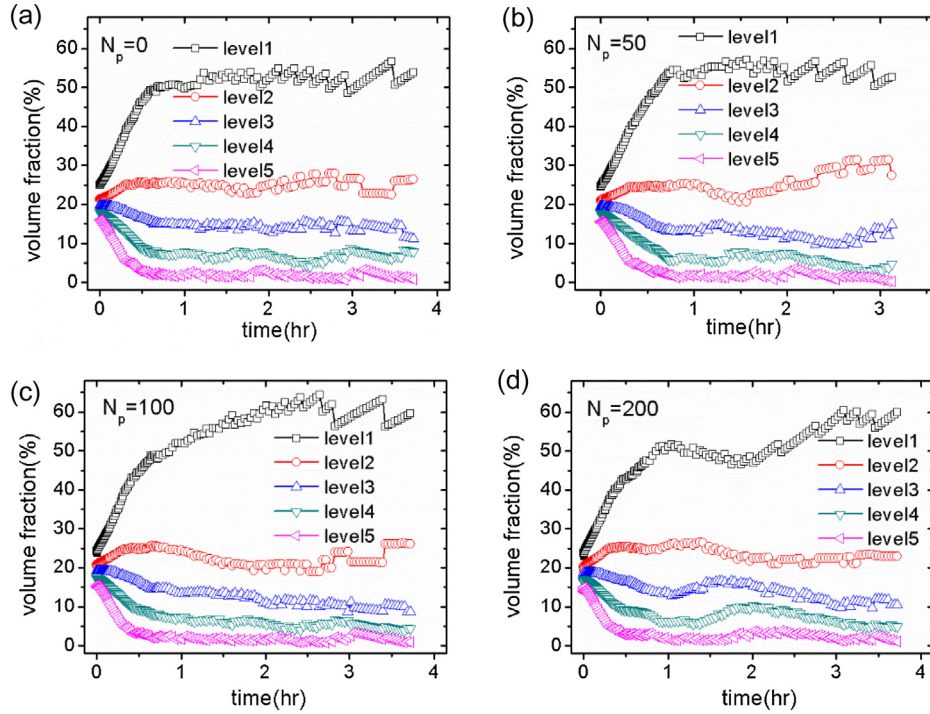


Fig. 5. Volume fractions of the five levels for $N_p =$ (a) 0, (b) 50, (c) 100, (d) 200.

sensitive to the different initial random grain constructions. To alleviate the interference from the random features of initial grain construction, instead, the ratio of average grain sizes between the largest group (level 1) and the whole system will be used to characterize the global abnormality of grain growth, denoted as χ .

The temporal evolution of χ at different porosities are plotted in Fig. 6(a). It can be seen from Fig. 6(a) that χ in the transition period $[0, 0.5]$ h increases rapidly to 1.3 regardless of porosity and then the distinction between different systems starts to show up. With increasing pore numbers, the deviation from the nonporous system appears to be larger in the time interval of $[0.5, 1]$ h except for the case with $N_p = 50$. Namely, the number of pores is the major factor that determines χ in the initial stage of grain growth. Nevertheless, when the sintering time is longer, the deviation does not follow the same trend any more. The system of $N_p = 100$ exhibits the highest χ of 1.7 when the time reaches 2.7 h. To better compare the results of χ between those of different porosities, the averaged abnormality χ_{ave} calculated during the steady period of evolution (approximately from 1 to 3 h) are plotted in Fig. 6(b). When there are no

pores, χ_{ave} is around 1.5, which can be interpreted by the classical theory of 3D ideally NGG [30]. Accordingly, the maximum grain size is 1.8 times of the average one $R_{g,ave}$. The distribution function $P(u)$ of grain sizes is [30]

$$P(u) = (2e)^\beta \frac{\beta u}{(2-u)^{2+\beta}} \exp\left(\frac{-2\beta}{2-u}\right) \quad (9)$$

where $u = R/1.25R_{g,ave}$ and $\beta = 3$ in the 3D system. Short calculation shows the average grain size of the largest 20% grains (level 1) is approximately 1.47 times of $R_{g,ave}$, which is very close to the current case of no pores. As the pore number increases, χ_{ave} increases rapidly at the low porosity and then reaches a maximum when $N_p = 100$ ($f_p = 1.3\%$). After that, χ_{ave} returns to the relative low level (~ 1.5). Therefore, it can be concluded that the AGG is affected by the total pore volume but not in a monotonous way. This can be rationalized as follows: when the porosity is low and the pore retarding effect is not significant, pore-boundary interaction including engulfment of pores may cause high AGG [5–7].

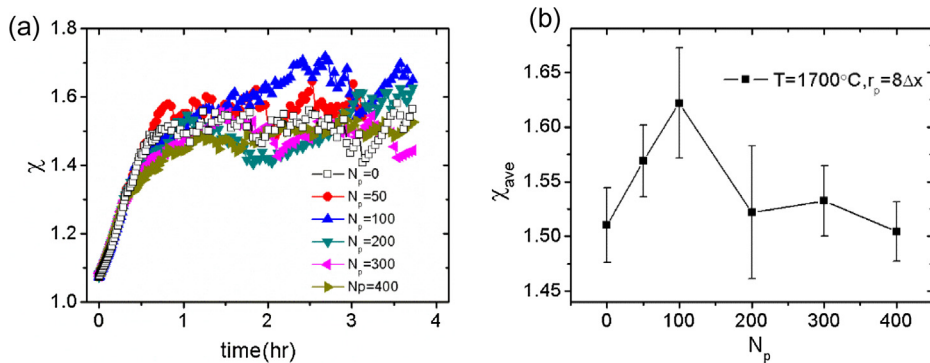


Fig. 6. Characterized abnormality χ with different pore numbers: (a) the evolution with time (b) the averaged value χ_{ave} in the time range of 1–3 h.

3.2. Individual pore size dependence

Aside from the total pore volume f_p , the grain growth dynamics is also expected to be related to the varying pore size r_p . In this section, the roles of pore sizes with several fixed f_p in the grain growth behavior are under investigation. Fig. 7 exhibits the evolution of the average grain radius $R_{g,ave}$ with time for the cases of $f_p = 1.3\%$ and $f_p = 5.1\%$ with different pore sizes r_p . It shows that the pore size indeed impacts the grain radius evolution, depending on f_p . For the case that f_p is as low as 1.3%, the grain growth dynamics curves of different pore sizes can hardly be distinguished from each other, as shown in Fig. 7(a), though some subtle difference found when $t > 3.2$ h. For the case of $f_p = 5.1\%$, different pore sizes lead to manifestly different grain growth behavior as plotted in Fig. 7(b). When r_p is large, the grain growth is rapid and approaching to that of NGG with no pores. When r_p is small, the grain growth is evidently stagnated. Thus, the effect of pores on grain growth dynamics highly relies on the number density of pores. Our simulation results are consistent with the experiments by Bourgeois et al. [16] that the more finely pores are divided, the more grain growth slows down.

Next, the effect of pore size on the abnormality of grain growth is explored. Analogue to Fig. 6(b), χ_{ave} for different r_p and f_p are compared and plotted in Fig. 8. Generally, χ_{ave} increases from $f_p = 0$ to $f_p = 1.3\%$ and decreases when $f_p > 2.6\%$. Especially, the largest χ_{ave} belongs to the smallest pore size at $f_p = 1.3\%$. As an overall trend, when f_p is small, low r_p leads to large abnormality and χ_{ave} is low for pores of large or intermediate sizes. For the systems with $f_p \geq 3.8\%$, small pores may suppress the χ_{ave} values as the grain growth is hindered by the pores. From the above results, we can see that increasing pore numbers for porous system or alternatively increasing pore sizes for less porous ones will generate more uniform grain distribution in general, that is, the uniform microstructure may be obtained with the existence of pores with appropriate size.

4. Discussion

According to the above results, it can be found that relative to the larger pores, the smaller ones may lead to worse AGG at low porosities and more significant stagnation of grain growth at high porosities. On the one hand, AGG has a close relationship with the detachment of pores from GBs (or the engulfment by grains) [32,33]. Consequently, AGG may be more likely to occur with smaller pores due to better capability of engulfment. On the other hand, the stagnation of grain growth depends on the mechanism concerning the interaction between GBs and pores. In accordance with Hillert [30], AGG is not likely to occur in a material where most of the pores are located at GBs. With the surface diffusion as the dom-

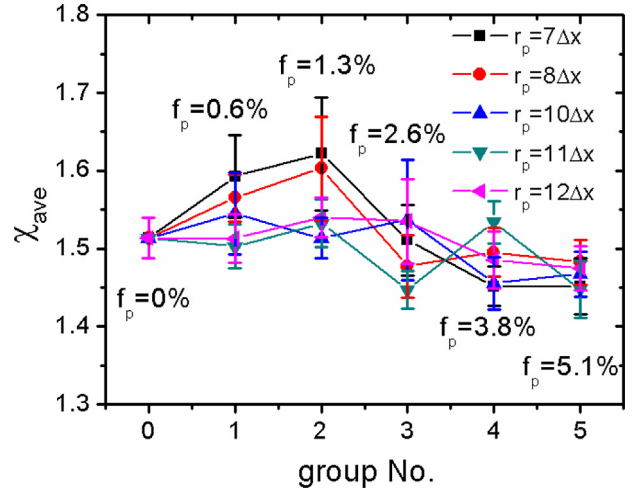


Fig. 8. Variation of χ_{ave} with respect to various r_p and f_p .

inant mechanism for UO_2 sintering [6], the effect of pores on grain growth should be examined via the analysis on the engulfment of pores by grains.

The numbers of pores in different levels of grains with $r_p = 8\Delta x$ are calculated, as shown in Fig. 9 in order to determine engulfment abilities of different grains. The grains in level 1 are the first ones to engulf pores whatever the number of pores and the corresponding rates are the highest. For the porous systems ($f_p = 2.6\%$ and $f_p = 3.8\%$), grains in level 1 are dominant in engulfing pores, however, for the less porous systems, ($f_p = 0.6\%$ and $f_p = 1.3\%$), the role of both level 1 and level 2 are determined to be significant. These again mean the impact of pore engulfment may be more important to less porous systems. Furthermore, the incubation times for the engulfment at different N_p are similar with each other, which can be attributed to the homogeneous pore size and the similarity in pore-GB interaction [9,29]. Similarly, Fig. 10 exhibits the evolution of pore number in grains for different pore sizes when $f_p = 1.3\%$. As indicated in Fig. 9, the smaller the pore size, the faster the engulfing of pores occurs.

4.1. Bi-grain system

To elaborate the above mechanisms, a bi-grain system is constructed in this study. Initially, one spherical grain A is embedded inside a matrix grain B and n_p pores (i.e. the number of pores per boundary) are arranged in grain A near the GB with the equal distance (e.g. $2\Delta x$), as shown in Fig. 11(a). Specifically, initial radius

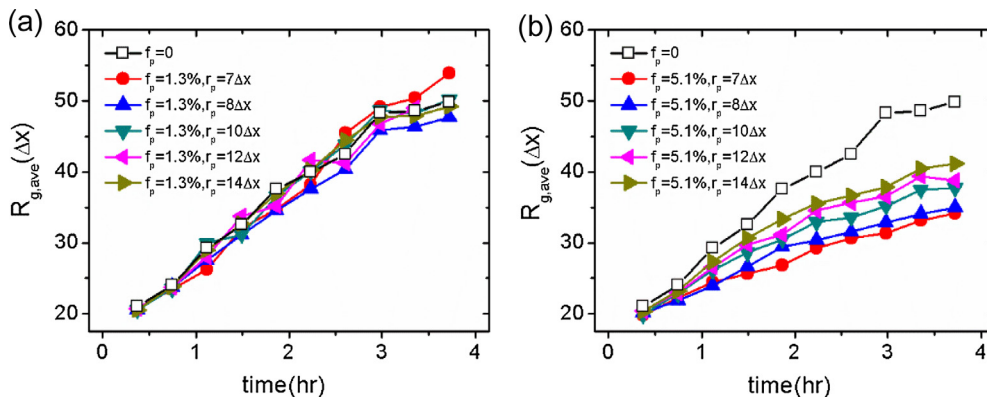


Fig. 7. Temporal evolution of $R_{g,ave}$ with pores of different sizes at (a) $f_p = 1.3\%$, (b) $f_p = 5.1\%$, respectively.

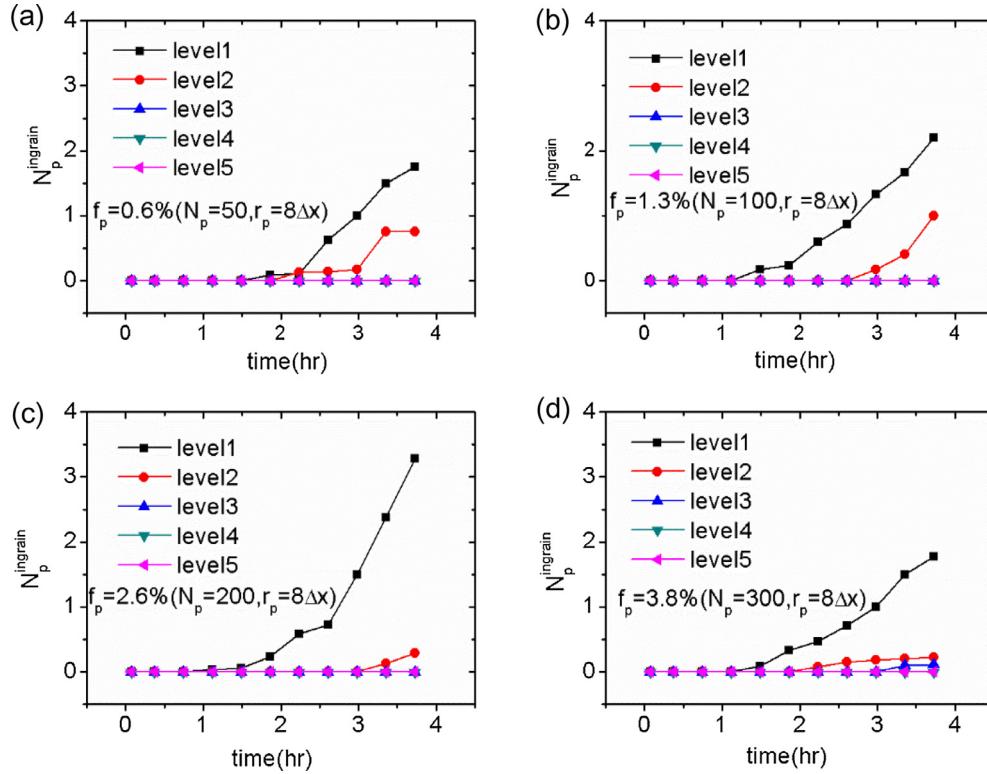


Fig. 9. Variation of number of pores ($r_p = 8\Delta x$) $N_p^{ingrain}$ in grains at five levels of f_p and N_p , (a) $f_p = 0.6\%$, $N_p = 50$, (b) $f_p = 1.3\%$, $N_p = 100$, (c) $f_p = 2.6\%$, $N_p = 200$, (d) $f_p = 3.8\%$, $N_p = 300$.

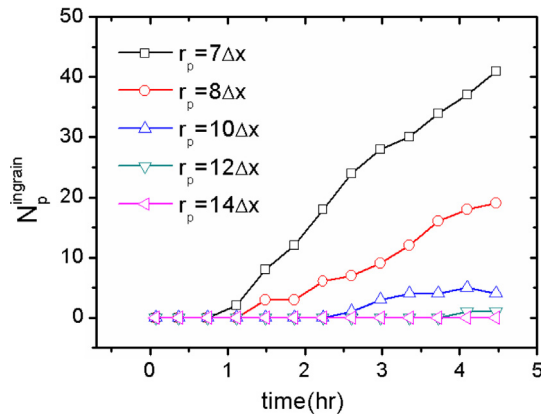


Fig. 10. Variation in number of pores in grains $N_p^{ingrain}$ for different pore sizes at $f_p = 1.3\%$.

R_g^A of grain A is $30\Delta x$, which means that pores start to contact with GB when $R_g^A = (30 - 2)\Delta x$. As time evolves, the inner grain A shrinks and the outer grain B grows, with pores being crossed by the GB. In order to illustrate the enlargement of grain B, an effective grain radius (R_g) is defined as follows. The centroid of grain B is assumed as one of the vertices of the cubic simulation box which are identical in the periodic frame, such as point O in Fig. 11(b). The grain radius of grain B, R_g , is calculated by averaging the distances between the point O and all the GB points. In particular, it should be noted that when the pores are situated at crossing GB, the corresponding part in GB will become the surface between the grain and the pores, which will be counted in the radius calculation as well.

The changes in the radius of grain B with different n_p when $r_p = 8\Delta x$ are plotted in Fig. 12. At the very early stage ($t < 0.15$ h), the grain radius with non-zero n_p is larger than that with $n_p = 0$. After a period of time, the radii for porous grains are lower than that of the non-pore grain. In fact, the changes in the grain radii are related to the rearrangement caused by the GB-pore interactions. Taking the typical case of $n_p = 12$ as an example, the GB shape changes can be found from the insets (denoted as a1-a4) of Fig. 12 for x-z slice snapshots as in Fig. 11(a) at four times: 0, 0.05, 0.22 and 0.3 h, respectively. At the very beginning, the GB plane is perfectly spherical as a1. In a short time, the GB migrates under the driving force of GB curvature. Especially, the GB near pores moves in a faster way than other parts to form TJs between pores and GBs from our simulation, resulting in the larger radius of grain B than the non-pore case as a2. In fact, these faster migration is consistent with the 2D phase field simulation by Tonks et al. [17]. Consequently, the more the pore number, the larger the grain radius. When the pores are located on GBs, the TJs between the GB and pores have been formed as a3. In this case, the GB can be regarded as being pinned by the pores, resulting in the close or smaller radius than that of the $n_p = 0$ case. As the GB migrates, after a longer time, the pores are about to detach from the GB and will be engulfed by grain B entirely. At this moment, the structure is illustrated by a4, when there is a critical point in the curves of grain radius evolution. After the critical point, the GB is free of pores, and the grain radius of grain B increases suddenly and approaches the non-pore case. The grain radius and time corresponding to the critical point are respectively denoted as R_{crit} and t_{crit} which will change with different pore distributions.

Fig. 13 summarizes the variation of R_{crit} with n_p and t_{crit} with porosities calculated by $f_p = 4\pi r_p^3 n_p / 3V$ with $V = 10^6 \Delta x^3$ as the volume of simulation box. In Fig. 13(a), the critical radii R_{crit} at the same n_p but different pore sizes r_p are almost the same, indicat-

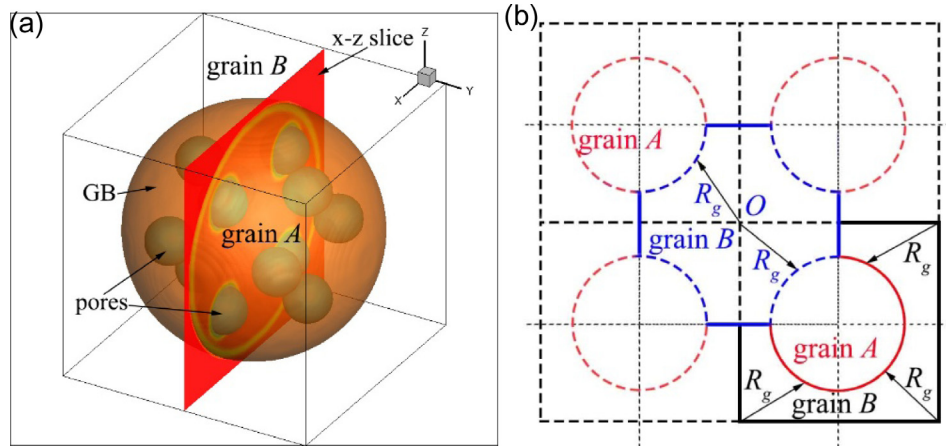


Fig. 11. Schematic pictures of (a) bi-grain system and (b) definition of R_g in grain B.

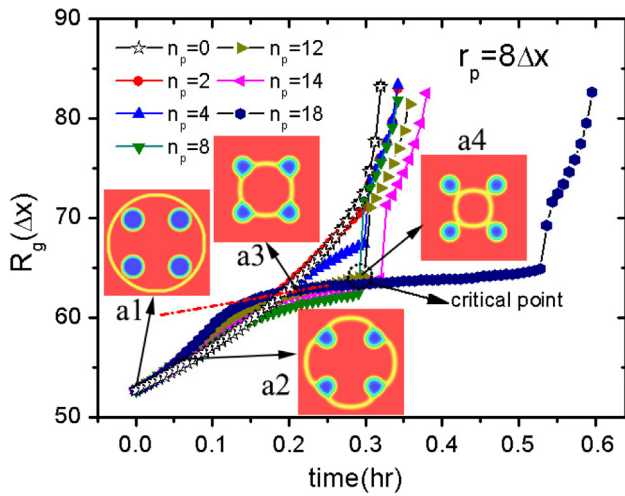


Fig. 12. Evolution of R_g when the embedded grain shrinks in the matrix grain with pores of $r_p = 8\Delta x$ and different n_p . Pictures (a1–a4) in the inset corresponding to the times: 0, 0.05, 0.22 and 0.31 h for $n_p = 12$. The red dash-dotted line shows an example of calculating the linear fitting of the slowest GB migration dragged by pores for $n_p = 18$. (For interpretation of the references to colour in this figure legend, the reader is referred to the web version of this article.)

ing that the r_p has a trivial effect on R_{crit} , which is not the case for n_p . When n_p is small, e.g. smaller than 8, R_{crit} decreases with increasing n_p . It is reasonable in that R_{crit} is related to the distance between pore-grain boundary and the centroid of the grain upon

pore detachment. This trend can well correspond to the AGG behavior of $N_p = 0, 50, 100$ shown in Fig. 6(b). Not surprisingly, in a system where there are continuous source of pores to be engulfed, the AGG induced by inhomogeneous pore distribution can occur consecutively and become remarkable. While n_p in Fig. 13(a) increases further, a large portion of GBs are covered by pores and R_{crit} is found to increase slightly and remains at a low level after the minimum is reached. Apparently, this is consistent with the latter part of Fig. 6(b). The results are likely to mean interactions between pores become influential at high porosity that may cause flattening of pores and retarding effect on grain growth, resulting in less abnormality.

In order to quantitatively determine the stagnation effect of pores on grain growth, the dependence of critical time t_{crit} on different r_p and porosities is predicted as shown in Fig. 13(b). When the porosity is low and the interaction between pores may be negligible, the larger pores show slightly higher t_{crit} . The difference is readily understood since the larger the pore, the longer time it needs to engulf the pore. However, the number of pores is lower when the pore size is larger under a given porosity and thus less pore-boundary interactions and engulfment events occur in the system with large pores. This leads to the weak influence of grain size on the grain growth rate in a poly-grain system at low porosity (also see Fig. 7(a) in Section 3). When the porosity is high, t_{crit} of smaller pores can be far larger than the larger ones. For example, t_{crit} of $r_p = 7\Delta x$ rises very quickly with porosity, indicating a strong retarding effect. Hence, when the coverage of the GB by pores is large, i.e. some pores are in close distances located on a GB and interaction between pores occurs, the curvature of GB as the driv-

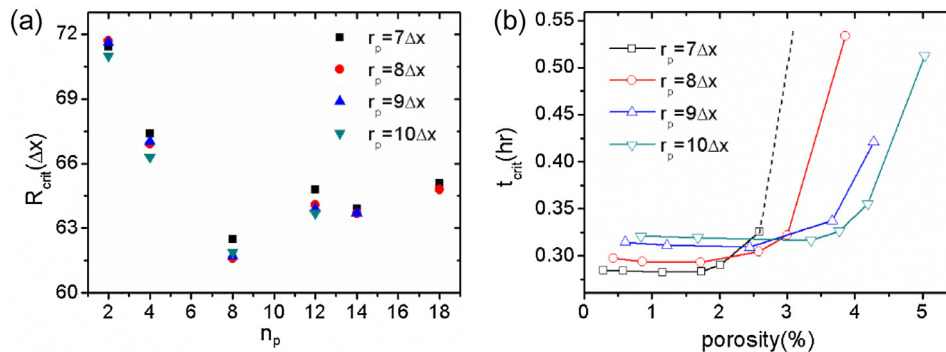


Fig. 13. The variations of (a) Critical grain radius R_{crit} with different n_p and (b) critical time t_{crit} with different porosities at varied r_p . In (b), the slash line shows the trend of very large t_{crit} with high porosities at $r_p = 7\Delta x$.

ing force of grain growth is significantly suppressed. In fact, the rest area in GB may even become nearly plain, analogous to the case that the GB between two TJs in nanocrystalline materials is almost plain[34] according to the Young's equation. From the Fig. 13(b), as the porosity increases to an appreciable amount, t_{crit} can be extremely long, e.g., when $r_p = 10\Delta x$ and $n_p = 14$, t_{crit} will be beyond 70 h (corresponding to $1,000,000\Delta t$, the maximum calculation steps in our simulation), which can be reasonably regarded as the stagnation of grain growth. This explains that smaller pores has a stronger hindering effect on grain growth at high porosities, which provides an explanation for Fig. 7(b).

4.2. Engulfment criterion

The influence of pores on GB migration can be investigated in terms of Zener's effect which describes the interaction between immobile particles and migrating boundaries. In Zener's description, there are several key assumptions: (a) the passage of the boundary does not alter the particle-boundary interaction, (b) the contacts between particles and boundaries are completely random, (c) each particle exerts the maximum pinning force on the boundary regardless of contact position. Specifically, for spherical particles the force F_p acting on the particle-boundary interface is

$$F_p = 2\pi r_p \gamma_b \cos \theta \sin \theta, \quad (10)$$

where r_p is the particle radius, γ_b is the boundary energy and θ is the drag angle. So, the maximum dragging force occurs when $\theta = \pi/4$. The velocity of boundary is

$$v_b = M_b(F_b - P_r) = M_b(F_b - \varphi_p F_p) \quad (11)$$

where M_b is the intrinsic boundary mobility (free of particles), $F_b = \alpha\gamma_b/R_b$ is the intrinsic driving force (or pressure) of the boundary due to its curvature with α being a geometric factor ($\alpha = 2$ for spherical grains) and R_b the curvature radius of boundary, $P_r = \varphi_p F_p$ is the resistive pressure due to the pore drag effect and φ_p is the number of pores per unit GB area. Based on Eq. (11), two extreme situations will occur for the interaction between immobile particles and the boundary i.e. $F_b \gg P_r$ and $F_b = P_r$. For the former case, the boundary will leave the particle behind, resulting in engulfment of particles by grains. For the latter one, boundary will be hindered by the particle, lead to the stagnation of grain growth. However, the application of Zener's theory to our results may not be straightforward because the pores can be mobile [8]. In fact, Ahmed et al. [8] extended Zener's theory to describe the interaction between mobile particle, i.e., pores, and boundaries by introducing the velocity of pores as

$$v_p = M_p F_p, \quad (12)$$

where M_p denotes the intrinsic mobility of pores. In this scenario, boundary will leave the pores behind and the engulfment of pores by grains can occur when $v_b > v_p$, which can be equivalently converted to

$$\varphi_p < \frac{F_b}{F_p} - \frac{M_p}{M_b}, \quad (13)$$

Moreover, consistent with our bi-grain results, φ_p can be represented by $\varphi_p = n_p/4\pi R_b^2$. Thus, a criterion of pore engulfment is established in terms of n_p . We can find the minimum upper bound of n_p , i.e., n_p^{UB} estimated as

$$n_p^{UB} = \min \left\{ 4\pi R_b^2 \left(\frac{F_b}{F_p} - \frac{M_p}{M_b} \right) \right\} \quad (14)$$

It can be inferred that engulfment may occur when $n_p < n_p^{UB}$. After investigating the right hand side (RHS) of Eq. (14), we can

find that the RHS will be minimum when $\theta = \pi/4$ that is consistent with Zener's assumption. Now, the RHS becomes a function of R_b and r at constant temperature for UO_2 . A diagram of n_p^{UB} with respective to R_b and r_p is depicted as shown in Fig. 14.

In our poly-grain system, the average grain radius grows from $22\Delta x$ to more than $50\Delta x$ with pores randomly distributed in the system. Initially, the maximum ratio of pore number to grain number is around 2, which is much smaller than the lowest n_p^{UB} of greater than 10, indicating that the engulfment can occur initially. Considering the randomness of pore distribution, the surroundings of GB will not change too much and the engulfment will continue to occur as the initial. For the bi-grain system, n_p^{UB} is estimated and compared with the maximum n_p used by taking the smallest grain A radius for $r_p = 7 - 10\Delta x$, as shown in Table 3. Obviously, n_p values studied in this work are all below n_p^{UB} , demonstrating that engulfment may be the dominant process in our systems. In fact, increasing n_p further will result in the stagnation of grain growth not co-movement of the pores and boundary. According to results of Ahmed et al. [8], this co-movement can be achieved in 2D or equivalently in cylinder grains with very high pore mobility. However, this can be hardly possible in our case, since (a) pore mobility is very low compared to GB mobility, (b) grains are closer to spheres not cylinders especially with irregular distribution of pores. In addition, the engulfment is difficult for a large number of pores due to the pore network. Finally, the stagnation of grain growth occurs for the very high porosities. In fact, our simulation results can be alternatively interpreted by resistive pressure model proposed by Tonk et al. [17], which can be found in the [supplementary material](#).

In this work, we have combined the effects of porosity and pore size to analyze the AGG in the final stage of UO_2 sintering considering the engulfment of pores by grains. When the porosity is low, the larger pore size causes the fewer pore number, reflected by the larger critical grain radius, and thus the grain growth is more likely to be normal rather than abnormal and vice versa. Given an appreciable porosity, if the pore number is large, the critical time is long and the grain growth is significantly suppressed, leading to lower

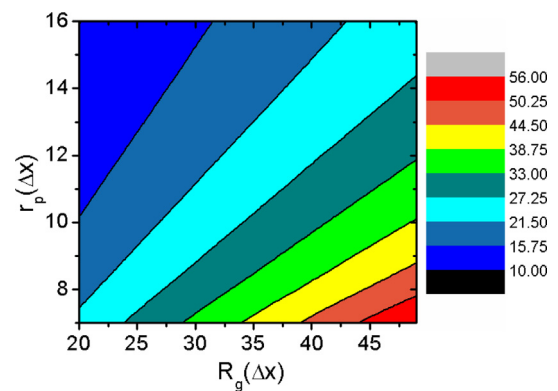


Fig. 14. Diagram of n_p^{UB} for pore radius r_p and grain radius R_g for engulfment criterion.

Table 3
Comparison of n_p in the bi-grain system.

r_p (Δx)	Smallest R_g^A (Δx) with pores	n_p^{UB}	Maximum n_p used
7	21	24	18
8	20	20	18
9	19	16	14
10	18	14	12

abnormality. Recent studies show that pore coalescence can occur depending on the distribution of pores in the final stage of sintering [35]. According to our results, coalescence results in larger pores and less interfaces, which can improve the uniformity of grains, especially when the porosity is not high.

5. Conclusion

We have employed the phase field model to study the grain growth behaviors of UO_2 with different pore distributions in the final stage of sintering. Our simulation results show excellent agreement with the relevant theories and experimental works. The dynamics of grain growth is found to strongly depend on the porosity and individual pore sizes. When there are no pores, NGG occurs as expected with the characteristics consistent with the classical theories of ideally 3D NGG. For the case of low porosities, AGG occurs preferentially with low pore sizes and the maximum abnormality is found with $f_p = 1.3\%$ at $r_p = 8\Delta x$. When the porosity is high (e.g. higher than 2.6%), grain growth is evidently suppressed because of the retarding effect of pores especially for smaller pores. Furthermore, the mechanism of AGG and stagnation of grain growth with pores are elucidated with R_{crit} and t_{crit} corresponding to the engulfment of pores. Specifically, the degree of AGG can be reflected by R_{crit} ; if the number of pores per GB is high, t_{crit} for engulfment of pores can be long which may even result in the stagnation of grain growth. On the whole, large and uniform distributed UO_2 grains can be obtained with low porosities and large pore sizes. The present work is expected to provide a theoretical background to control the microstructure of UO_2 . Further studies are suggested to be performed on the grain growth with GB anisotropy [36] and mechanisms including more interactions of pore-boundary, such as GB-diffusion and evaporation-condensation mediated pore migration which can help study pore coarsening.

Acknowledgement

The authors acknowledge the financial support from the National Key Research and Development Program of China (Grant Nos. 2016YFB0700100 and 2016YFB0700901), the National Natural Science of Foundations of China (Grant Nos. 51372046, 51479037, 91226202 and 91426304), the Major Project of the Ministry of Science and Technology of China (Grant No. 2015 ZX06004-001), Key Research Program of Frontier Sciences, CAS (Grant No. QYZDB-SSW-JSC037), China Postdoctoral Science Foundation (Grant No. 2017M612045), the Ningbo Municipal Natural Science Foundation (Grant No. 2014A610006), One Thousand Youth Talents plan, the key technology of nuclear energy, 2014, CAS Interdisciplinary Innovation Team and K.C.Wong Education Foundation (rczx0800). The authors also acknowledge the support of

Special Program for Applied Research on Super Computation of the NSFC-Guangdong Joint Fund (the second phase) (U1501501 to Juan Li and Aiguo Wu) and ITaP at Purdue University for computing resources.

Appendix A. Supplementary material

Supplementary data associated with this article can be found, in the online version, at <https://doi.org/10.1016/j.commatsci.2017.12.057>.

References

- [1] J.A. Turnbull, J. Nucl. Mater. 50 (1974) 62–68.
- [2] J.B. Ainscough, B.W. Oldfield, J.O. Ware, J. Nucl. Mater. 49 (1973) 117–128.
- [3] J.R. MacEwan, J. Am. Ceram. Soc. 45 (1962) 37–41.
- [4] R.J. Brook, J. Am. Ceram. Soc. 52 (1969) 56–57.
- [5] K. Ahmed, C.A. Yablinsky, A. Schulte, T. Allen, A. El-Azab, Model. Simul. Mater. Sci. Eng. 21 (2013) 065005–065027.
- [6] K. Ahmed, J. Pakarinen, T. Allen, A. El-Azab, J. Nucl. Mater. 446 (2014) 90–99.
- [7] K. Ahmed, T. Allen, A. El-Azab, J. Mater. Sci. (2016) 1–17.
- [8] K. Ahmed, M. Tonks, Y. Zhang, B. Biner, A. El-Azab, Comp. Mater. Sci. 134 (2017) 25–37.
- [9] L. Bourgeois, P. Dehadt, C. Lemaignan, J.P. Fredric, J. Nucl. Mater. 295 (2001) 73–82.
- [10] G.T. Higgins, Met. Sci. 8 (1974) 143–150.
- [11] A.D. Rollett, D.J. Srolovitz, M.P. Anderson, Acta Metall. 37 (1989) 1227–1240.
- [12] B.-K. Lee, S.-Y. Chung, S.-J.L. Kang, Acta Mater. 48 (2000) 1575–1580.
- [13] J. Deng, S. Rokkam, Mater. Trans. 52 (2011) 2126–2130.
- [14] M. Hillert, Acta Metall. 36 (1988) 3177–3181.
- [15] S.G. Kim, Y.B. Park, Acta Mater. 56 (2008) 3739–3753.
- [16] L. Bourgeois, P. Dehadt, C. Lemaignan, A. Hammou, J. Nucl. Mater. 297 (2001) 313–326.
- [17] M.R. Tonks, Y. Zhang, A. Butterfield, X.-M. Bai, Model. Simul. Mater. Sci. Eng. 23 (2015) 045009–045024.
- [18] Y. Li, S. Hu, R. Montgomery, F. Gao, X. Sun, Nucl. Instr. Meth. Phys. Res. B 303 (2013) 62–67.
- [19] Y. Zhu, H. Hallberg, J. Nucl. Mater. 467 (Part 1) (2015) 113–120.
- [20] P.V. Nerikar, K. Rudman, T.G. Desai, D. Byler, C. Unal, K.J. McClellan, S.R. Phillpot, S.B. Sinnott, P. Peralta, B.P. Uberuaga, J. Am. Ceram. Soc. 94 (2011) 1893–1900.
- [21] H.Z. Fang, Y. Wang, S.L. Shang, D.J. Paul, Z.K. Liu, J. Phys.: Condens. Matter 24 (2012) 225001–225005.
- [22] M.N. Kelly, S.A. Bojarski, G.S. Rohrer, J. Am. Ceram. Soc. 100 (2017) 783–791.
- [23] S.M. Foiles, Scripta Mater. 62 (2010) 231–234.
- [24] P.S. Maiya, J. Nucl. Mater. 40 (1971) 57–65.
- [25] S.G. Kim, D.I. Kim, W.T. Kim, Y.B. Park, Phys. Rev. E 74 (2006) 061605–061618.
- [26] F. Aurenhammer, ACM Comput. Surv. 23 (1991) 345–405.
- [27] R.J. White, M.O. Tucker, J. Nucl. Mater. 118 (1983) 1–38.
- [28] H.V. Atkinson, Acta Metall. 36 (1988) 469–491.
- [29] R.M. German, Crit. Rev. Solid State 35 (2010) 263–305.
- [30] M. Hillert, Acta Metall. 13 (1965) 227–238.
- [31] K.-J. Ko, P.-R. Cha, D. Srolovitz, N.-M. Hwang, Acta Mater. 57 (2009) 838–845.
- [32] I.W. Chen, G.N. Hassold, D.J. Srolovitz, J. Am. Ceram. Soc. 73 (1990) 2865–2872.
- [33] Ouml, J. Tzer, V. Rehn, W. Rheinheimer, M.J. Hoffmann, B. Nestler, J. Ceram. Soc. Jpn. 124 (2016) 329–339.
- [34] G. Gottstein, L.S. Shvindlerman, B. Zhao, Scripta Mater. 62 (2010) 914–917.
- [35] Y. Xiong, J. Hu, Z. Shen, J. Eur. Ceram. Soc. 33 (2013) 2087–2092.
- [36] Y. Guo, J. Wang, Z. Wang, S. Tang, Y. Zhou, Comp. Mater. Sci. 88 (2014) 163–169.